ATLAS Inner Detector Performance

Nektarios Ch. Benekos
Roger Clifft
Markus Elsing
Alan Poppleton
European Organization for Nuclear Research - CERN

Abstract

Two ATLAS reconstruction packages, iPatRec and xKalman, running within the ATHENA framework using software release 6.0.3, have been used to study the performance of the ATLAS Inner Detector. Two versions of the detector layout, have been used namely the version currently used for DC1 and the version foreseen for DC2. The response of the detector for single muons has been measured to obtain the track parameter resolution and quality. More realistic performance figures for the detector and a measurement of the pattern recognition capabilities of the algorithms have been obtained from a further study with di-quark jets, including pile-up. The results obtained with the two algorithms, and the two layouts have been compared. A comparison with the results presented in the Physics TDR has found some degradation in performance which is attributed to changes in the layout geometry and the addition of more material.

1 Introduction

A performance study of the ATLAS Inner Detector has been made using the Offline Software Release 6.0.3 of the reconstruction algorithms iPatRec[1] and xKalman[2].

Two layouts of the detector have been used; the DC1 layout for which there is a lot of existing data from the DC1 data challenge, and the so called Initial layout where the intermediate pixel layer and part of the end-cap TRT have been removed.

An outline of the Inner Detector, some details of the layouts, and a table of geometrical parameters, including those of the physics TDR layout, are given in Section 2.

A brief description of the two reconstruction algorithms follows in Section 3, including some introductory comments on their input parameters which originate from different event data models and different detector descriptions. Reasons for this and the implications are also discussed.

Section 4 gives some simple but realistic parameterizations of resolutions which are later compared with data.

Results for impact parameter and transverse momentum resolutions of single particles are presented in Section 5. Muons have been used, as they allow a study of the optimum values achievable. The behaviour of the resolutions as a function of $|\eta|$, for both algorithms and both layouts are presented and discussed in detail. A comparison of the results with those of the physics TDR, has shown the subsequent evolution of the resolutions.

A study of tracks in jets, with and without the addition of pile-up is presented in Section 6, for both algorithms and both layouts. The efficiency of track finding and the quality of the found tracks, as well as the track resolutions, have been obtained. Here again, the results are compared with those presented in the physics TDR.

Finally, in Section 7, some conclusions are drawn.

2 The ATLAS Inner Detector

The ATLAS Inner Detector, is shown in Figure 1. It combines high resolution silicon detectors at inner radii with a transition radiation detector at outer radii. The whole device is contained within a superconducting solenoid which provides an axial magnetic field of nominal strength 2T. A full description of the detector is given in the ATLAS Physics TDR[3]. Three types of sub-detectors are involved:

- **Silicon Pixel detectors**. These are high granularity devices located on concentric cylinders in the barrel region and on discs in the end-cap regions ; the number of cylinders and discs being 3 in the DC1 layout and 2 in the Initial layout. The Initial layout has a coarser pixel granularity in the innermost layer. The detectors provide a high precision set of two dimensional measurements close

to the interaction point which are especially important for heavy flavor tagging. A more complete description is given in [4] .

- **Silicon Microstrip detectors(SCT)**. The SCT consists of rectangular detector modules located on 4 concentric cylinders in the barrel region, and 9 discs supporting trapezoidal (projective) modules in the end-caps. The detector provides a nominal 4 stereo pairs of precision measurements per track at intermediate radii. With their high granularity and low occupancy, the detectors combine well with the pixels to provide measurements of track momentum, impact parameter, and vertex position. More technical details are given in [5]

- **Transition Radiation detector(TRT)**. The TRT is made up of many layers of straw tubes, positioned parallel to the beam axis in the barrel region and radially in the end-caps. Layers of radiator are interposed between straw tube layers to create transition radiation. An average of 31 measurements per contained track are obtained in the barrel and 33 per track in the end-caps. The TRT makes a significant contribution to the overall track momentum precision as well as providing an inherent electron identification capability.

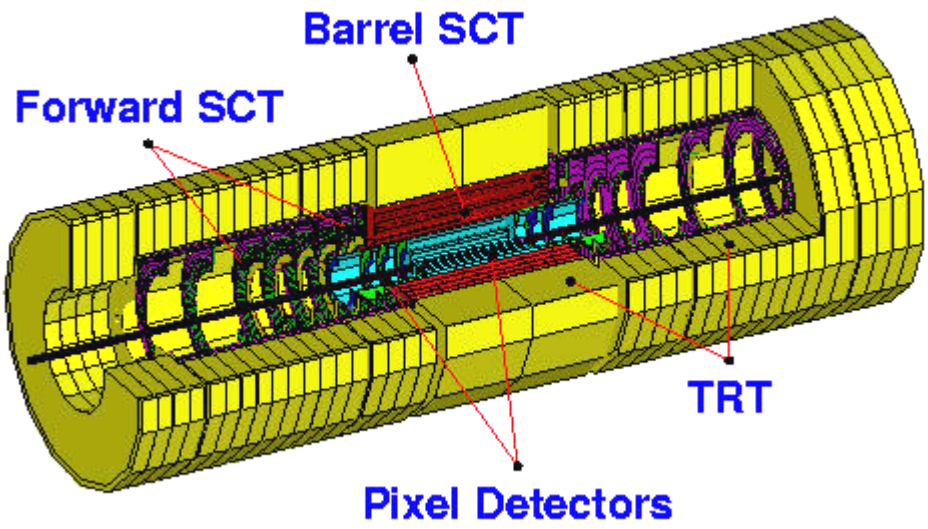

Figure 1: Three-dimensional view of the ATLAS Inner Detector.

2.1 The Inner Detector Layout

The Inner Detector layout has been continuously evolving as a result of engineering developments and more recently for cost reasons. Since the time of the Physics TDR[3], small shifts have occurred to the positions and dimensions of the SCT and TRT, but major changes have been made to the Pixel system, in particular to the innermost layer, the B-layer. The radius of the B-layer has been increased in order to accommodate a larger beam pipe and the whole Pixel detector has been given an independent insertion

	Physics TDR layout	Insertable DC1 layout	Initial layout
b-layer R (cm)	4.0	5.05	5.05
layer-1 R (cm)	11.0	8.85	staged
layer-2 R (cm)	14.2	12.25	12.25
Tilt angles (deg)	-9.5	-20.0	-20.0
Tilt angles b-layer (deg)	-10.5	-20.0	-20.0
dz/dR angles (deg)	0.0	1.1	1.1
Pitch Rϕ (μm)	50.	50.	50.
Pitch Z (μm)	300.	400.	400.
Pitch Z b-layer (μm)	300.	300.	400.
Big pixels (μm)	no	600.	600.
Big pixels b-layer (μm)	no	500.	600.
Ganged pixels (μm)	no	yes	yes
Sensor thickness (μm)	150	250.	250.
Sensor thickness b-layer (μm)	150.	200.	250.
Number of disks	4	3	2

Table 1: Evolution of the Pixel layout.

capability so that it can be inserted late or replaced if damaged by radiation. This latter development has caused a serious increase in the amount of material, with the pixel-barrel radiation-thickness increased by 50% and a significant support structure shadowing the complete SCT and TRT end-cap regions. Detail changes have been made to the pixel granularity with regular bands of larger pixels and non-adjacent bands of ganged channels. The relevant pixel parameters for the different layouts are listed in Table1.

The two layouts studied in this report are the so-called DC1 and Initial layouts. The former was used since a lot of data generated for Data Challenge 1 was available, also it provided a more up-to-date layout than that used in the Physics TDR. The latter is the layout currently foreseen for the initial data-taking period.

3 Inner Detector Software

The present study was performed on the data generated for DC1 using Atlsim[7] from Atlas software release 3.2.1 . Reconstruction was run under the Athena[8] framework from software release 6.0.3 . Two reconstruction packages were used, namely, iPatRec[1] and xKalman++[2]. These packages were run with the default configuration options provided for 6.0.3 .

Release 6.0.3 is the production release provided for the DC1 reconstruction phase and for HLT (High Level Trigger) studies of the offline performance. In principle, the offline reconstruction input data should have been taken from Raw Data Objects (RDO) - a C++ representation of the bytestream which will be recorded by the Atlas Data

Acquisition [9]. In practice, to economize data storage, the RDO structure was obtained by conversion from the previous Event Data Model (EDM), the so-called 'RD Event', in a preliminary job step during the Athena execution. At the time of the 6.0.3 release, neither iPatRec nor xKalman++ had fully completed their migration from this previous EDM, which was still used by iPatRec for its TRT data, and by xKalman++ for its Silicon data input.

In addition, different Detector Description schemes were used by the two reconstruction packages. Development is underway to rationalize this situation and to provide an interface to an Alignment/Calibration database, but this will only become available on the DC2 timescale. Similarly, each package has its own model for the material distribution as no central package has yet been provided.

Some of the inconsistencies in the observed results are attributed to the status of the Event Data Models and Detector Descriptions used by the two algorithms.

3.1 iPatRec

iPatRec[1] consists of a modular set of algorithmic packages which perform tasks such as track finding (i.e. pattern recognition), track following (i.e. hit association), track fitting and extrapolation through an inhomogeneous magnetic field. These packages communicate through the iPatTrack data model.

At the initialization phase, iPatRec creates a geometry data-base describing the properties of each detector module in the precision tracker plus the module's relationship to a simplified material model. The track finding, following and fitting procedures make extensive use of this data-base. Another initialization task is to parameterize the magnetic field to enable a fast propagation of track parameters between layers.

In the first step of event reconstruction, adjacent raw-data channels are clustered, and space-points are produced from these clusters.

The general procedure is to form track-candidates using space-point combinatorials subject to criteria on maximum curvature and crude vertex region projectivity. Candidates then undergo a track-fit procedure to give track parameters with covariance at the point of closest approach to the beam-line (perigee parameters). The track follower algorithm propagates these parameters to form an intersect with error ellipse at each 'layer' in turn. Clusters are associated to the track from the traversed detectors.

Good quality track-candidates are retained for extrapolation to the TRT, where a histogramming technique is used to select the TRT hits to be added. Tight cuts are made on the straw residuals and on the ratio of found to expected straws, in order to limit high luminosity occupancy effects.

During a final fit, energy loss and Coulomb scattering are taken into account. Pixel clusters have two weighting possibilities: they are taken to be 'precise' when uniquely assigned and consistent with the cluster sizes and shapes most frequently observed for the appropriate track crossing angle; otherwise they are termed 'broad'. The error on a 'precise' centroid is taken to be 10 μm for the transverse component, with a

larger longitudinal error taken according to the pixel aspect ratio. A flat distribution is assumed for 'broad' clusters (i.e. the cluster width divided by $\sqrt{12}$). Single and double strip SCT clusters are assigned a 23 μm error to be consistent with test-beam measurements, otherwise they are assumed to follow a flat error distribution. TRT drift hits are assigned a 170 μm error.

A detector with an active area traversed without an associated cluster is classified as a 'hole' and retained for material and quality information. Accepted tracks are required to have at least 6 silicon clusters and a fit probability greater than 0.001. Tracks with cluster(s) in the 2 innermost pixel layers plus TRT association are termed primary tracks and are permitted a maximum of 3 holes. Otherwise a maximum of only one hole is allowed in the associated layers: truncated tracks have hits starting in the innermost layer but were not successfully followed to the outermost layers or TRT; secondary tracks start further out and are required to have TRT association. A track is not allowed to share more than 3 silicon clusters with any other track.

3.2 xKalman++

xKalman++[2] is a package for global pattern recognition and track fitting in the Inner Detector, to find charged tracks with transverse momentum above 0.5 GeV/c.

By default, the release 6.0.3 algorithm starts track reconstruction in the Silicon detector layers using a segment search. The initial track finding is performed in the Pixels and SCT and finds sets of space points defining primary trajectories. A subsequent step uses each set of space points as input for a Kalman filter smoother formalism which picks up all consistent clusters along the track in the silicon layers. Each reconstructed track is then extrapolated outwards into the TRT, where a narrow road is defined around the extrapolated trajectory. All TRT straw and drift time hits found within this road are then added for the final track finding and track fitting steps. An xKalman track candidate is retained for output if it satisfies the following cuts:

- number of silicon clusters > 7
- number of silicon 'holes' < 3
- maximum silicon 'gap' $= 2$
- ratio of TRT hits to crossed straws > 0.7
- the track has at least 5 uniquely assigned clusters.

3.3 Simulated Inefficiencies and Track Selection

Single channel noise and inefficiency were randomly generated in the simulation with similar specifications to those applied for the Physics TDR. Neither reconstruction package appears to be particularly sensitive to noise or inefficiency at these levels. For example, the track-finding efficiency for single high-energy muons in the DC1 layout is

99.8%, with most of the inefficiencies occurring for tracks from a displaced vertex or close to the high-η limit. For this data the mean number of silicon clusters is 11.6 per track. The corresponding numbers for the Initial layout are 10.5 silicon clusters per track with a track-finding efficiency of 99.5%.

Many physics analyses have applied a set of standard quality cuts to the tracks output from the reconstruction. The criteria for these were studied in the context of the Physics TDR. They strongly suppress fake tracks and help ensure that the retained tracks have the optimum parameter resolutions. For the silicon clusters, these cuts are:

- at least 9 silicon clusters
- at least one associated hit in the B-layer
- at least one associated hit in the other pixel layers

However, the evolution of the Inner Detector layouts has tended to reduce the robustness against detector inefficiencies. For the DC1 layout the above quality cuts remove 2.6% of high-energy muon tracks, for the Initial layout this rises to 8.8%. While the physics analysis groups may decide to relax these criteria, the current assumption on the level of simulated inefficiencies will cause an increase in the proportion of less well-measured tracks and hence degrade the average parameter resolutions more strongly for the Initial layout.

The results shown in Sections 5 and 6 are obtained without applying any selection cuts.

4 Parameterizations

4.1 Track Parametrization

The trajectory of a particle moving in a solenoid magnetic field B with no multiple scattering and negligible bremsstrahlung radiation, can be described by a set of 5 helix parameters P.

$$P = (d_0, z_0, \phi_0, cot\theta, Q/p_T) \tag{1}$$

where:
d_0 is the signed transverse impact parameter, ϕ_0 (azimuth) is the ϕ coordinate of the track in the xy plane at the point of closest approach to the origin, p^0 is the signed radius of the curvature (see Figure2). The longitudinal impact parameter z_0 is defined as the value of z of the point on the track that determines d_0. The parameter $cot\theta$, with θ the polar angle, gives the inverse slope of the track in the (r,z) plane. The parameter Q/p_T, with Q the charge of the particle, can be deduced from the measured radius of the curvature. This means that Q/p_T, and not p_T, is the quantity measured with Gaussian errors. In case of muons, a single Gaussian distribution can describe the distribution of the resolution of each track parameter. The contribution of tails in the distribution is negligible [11] .

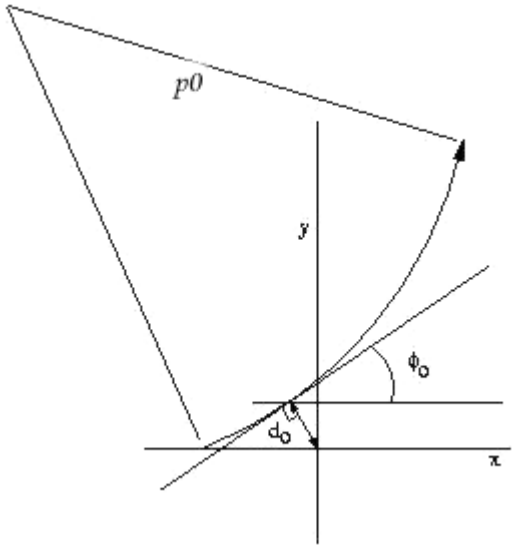

Figure 2: The helix parameters of a track moving through the bending plane of a uniform magnetic field.

4.2 Simple parametrization of impact parameter resolution

When the b-layer is present, the measurement of the impact parameters d_0 and z_0 depends predominantly on the first two measurements planes. In the case of two detection layers, the following analytic relation gives the approximate resolution of the impact parameters:

$$\sigma = \frac{r_1\sigma_2 \oplus r_2\sigma_1}{r_2 - r_1} \oplus \frac{k_1 r_1}{p_T} = A \oplus \frac{B}{p_T} \tag{2}$$

The position resolution of the first and second detector layers at r_1 and r_2 are given by σ_1 and σ_2 respectively. The term $k_1 p_T^{-1}$ describes the RMS of the multiple scattering angle at the first plane.

The term A represents the intrinsic error on the track parameter and B represents the multiple scattering error. Both A and B depend on $|\eta|$ but not on p_T. Therefore for at a fixed value of $|\eta|$, the matrices A and B can be determined via one measurement at high and one at low p_T. In the present studies A was determined for $p_T = 200$ GeV/c and B for $p_T = 1$ GeV/c.

The transverse momentum and pseudorapidity, η, of tracks in hadronic collisions are important parameters.

The uncertainty on $1/p_T$ as given in [12] is:

$$\sigma(1/p_T) = A_{p_T} \oplus \frac{B_{p_T}}{p_T\sqrt{sin\theta}} \tag{3}$$

In the absence of multiple scattering, the error on track curvature $(1/\rho)$ resulting from

N individual position measurements is constant and equal to [3] :

$$\sigma(1/\rho) = A_{p_T} = \frac{\epsilon}{L^2}\sqrt{C_N} \tag{4}$$

where:
ϵ is the error on each position measurement, L is the distance between the two end point measurements and C_N is a constant depending on the number and separation of the individual measurements points. With no energy loss, in a uniform field, B, the radius of curvature is $\rho = p_T/eB$ and hence :

$$\sigma(1/p_T) = A_{p_T} \cdot eB = eB\sigma(1/\rho) = \frac{eB\epsilon}{L^2}\sqrt{C_N} \tag{5}$$

In the presence of multiple scattering an additional term, $\frac{B_{p_T}}{p_T\sqrt{sin\theta}}$, must be added in quadrature to the measurement error.

4.3 Track Parameter Pull

The pull for track parameter α is defined as :

$$Pull(\alpha) = \frac{\alpha_{rec} - \alpha_{true}}{\sigma(\alpha)} \tag{6}$$

where:
$\sigma(\alpha)$ is the error of track fit parameter, α, of the diagonal elements of the error matrix.

4.4 Tail Fractions

A study of the fraction of tracks in the tails of the pulls of the 5 track parameters distributions has been made. The tail fraction in the transverse impact parameter distribution is defined as the fraction of the tracks where $|d_0^{reco} - d_0^{gen}| > 3\sigma(d_0)$, with an equivalent definition for the others track parameters. The resolutions used, are those obtained from fitting Gaussians to the cores of the distributions from each of the $|\eta|$ intervals.

5 Single Particle Results

In this section, the performance of the detector is evaluated by measuring the parameters of single muon tracks at several momenta. The results represent an idealization of what can be expected in normal LHC operation, independent of pattern recognition problems associated with multi-track events. The resultant resolutions are sensitive to several features of the layouts including the amount of material, the layer positions, and the pixel granularity. Since the Physics TDR performance measurements, the impact parameter resolution at low momentum has been substantially degraded by moving

the B-layer further out and increasing its thickness, hence its multiple scattering contribution. Furthermore, the pixel end-cap wheels are appreciably closer to the vertex, weakening the initial angle determination. In this case, since only the pixel and innermost SCT measurements are in the full-field region (roughly for tracks with $|\eta| > 2$), the sagitta determination, hence momentum measurement, is also weakened.

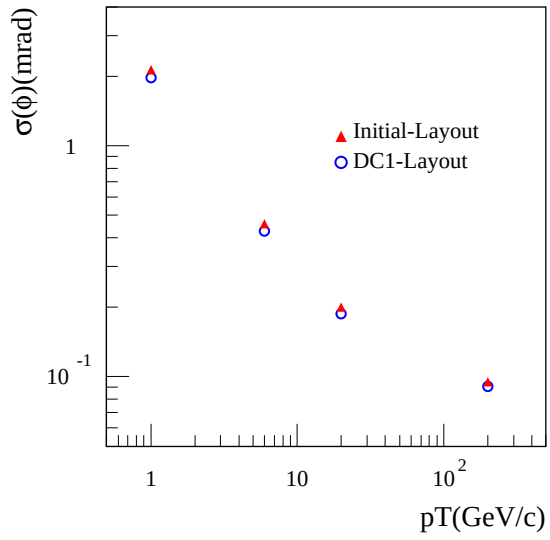

Figure 3: Angular resolution in ϕ of charged tracks as a function of p_T for $|\eta|$ <0.25 for both layouts (iPatRec).

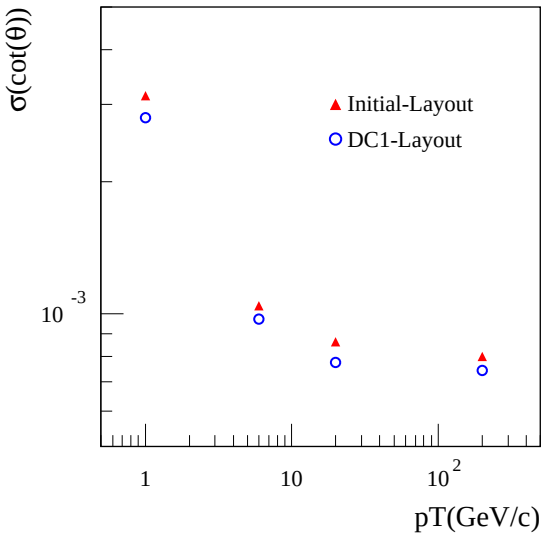

Figure 4: Angular resolution in $\cot\theta$ of charged tracks as a function of p_T for $|\eta|$ <0.25 for both layouts (iPatRec).

Two additional sources of degradation have been introduced for the Initial layout; namely, a reduction of the B-layer pixel granularity and the removal of the middle pixel layer. The removal of this layer would barely effect the resolutions if the remaining layers were completely hermetic and 100% efficient. However, the simulation leads to a significant number of tracks with only one pixel cluster, hence a degraded initial angle measurement. In addition, the tracks missing a B-layer cluster are less well-measured than their DC1 counterparts as the first measurement is farther from the vertex and the measured track-length shorter. The angular resolutions obtained for the DC1 and Initial layouts are shown for central tracks as a function of p_T in Figures 3 and 4. The effect of the reduction in the B-layer longitudinal granularity is apparent in the $\cot\theta$ resolution.

On average, there are 3 to 4 pixels forming a cluster in the DC1 B-layer, with the cluster size showing an $|\eta|$ dependence as the inclined tracks at higher $|\eta|$ produce clusters with larger longitudinal dimensions ($\sim$1 mm). A cluster centroid measurement is more accurate than that from a single pixel, with the larger clusters being more accurate in both dimensions. However, the improvement with increasing cluster size rapidly saturates. Thus, the decrease in B-layer pixel granularity for the Initial layout worsens the resolution, with the most significant effect being to the longitudinal component in the barrel region.

5.1 Transverse impact parameter resolution

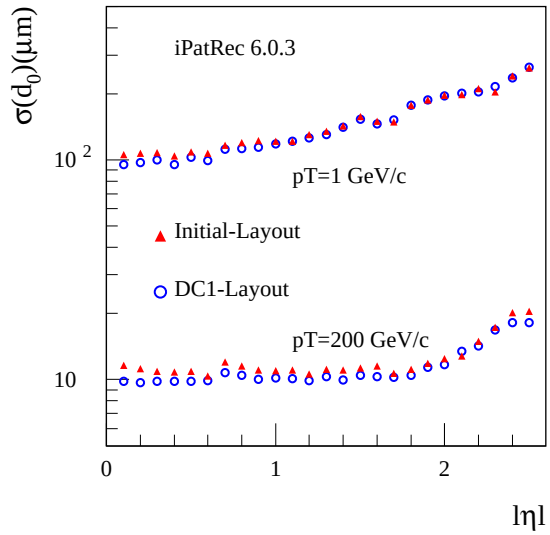

Figure 5: Transverse impact parameter resolution (d_0) as function of $|\eta|$ for muons of p_T = 1 GeV(upper) and p_T = 200 GeV(lower) for both layouts (iPatRec).

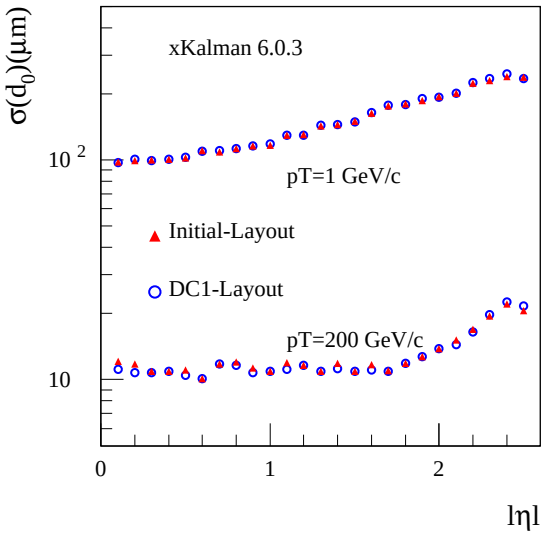

Figure 6: Transverse impact parameter resolution (d_0) as function of $|\eta|$ for muons of p_T = 1 GeV(upper) and p_T = 200 GeV(lower) for both layouts (xKalman).

A precise measurement of the transverse impact parameter of a track, d_0, is necessary for primary vertex association and the reconstruction of short-lived secondary vertices. These are essential for heavy flavor tagging and life-time measurements.

The resolution of the transverse impact parameter, expressed as a function of $|\eta|$ for the DC1 and Initial layouts, at p_T= 1 and 200 GeV/c, is given for iPatRec in Figure 5 and for xKalman in Figure 6.

It is seen that both algorithms and both layouts give results in fairly close agreement with each other.

For reasons of clarity, for these and subsequent figures, the error bars have not been shown. In general, there are of a similar magnitude to the symbol size(2-4%).

At high momentum, the resolution is almost constant up to $|\eta| \sim 1.8$, but then degrades rapidly in the end-cap region. The degradation is due to a reduction in the measured radial length for tracks longitudinally exiting the tracker which produces an increase in the relative distance to extrapolate back to the beam-line, and thus an increased extrapolation error.

At low momentum the resolution is much worse due to the dominant multiple scattering contribution from material up to and including the first measurement. There is also a continuous rise with $|\eta|$, since the material thickness of the beam-pipe and B-layer increase with $\sin\theta$.

The ratio of the transverse impact parameter resolution, iPatRec/xKalman, for the DC1 and Initial layouts, at p_T= 200 and 1 GeV/c, is shown in Figures 7 and 8. The

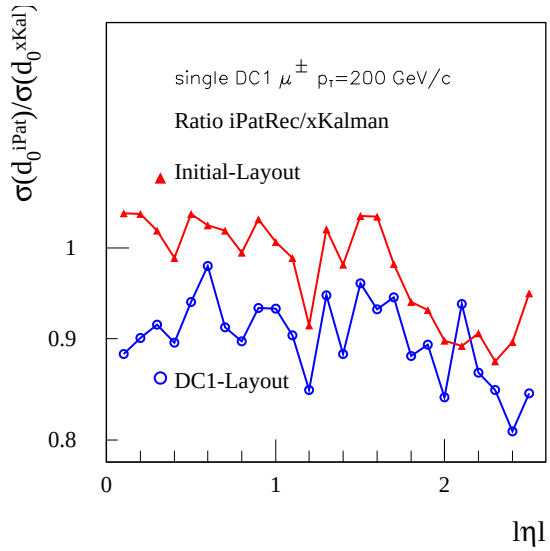

Figure 7: Ratio of d_0 resolution iPatRec to xKalman for $p_T = 200$ GeV for DC1 and Initial layout.

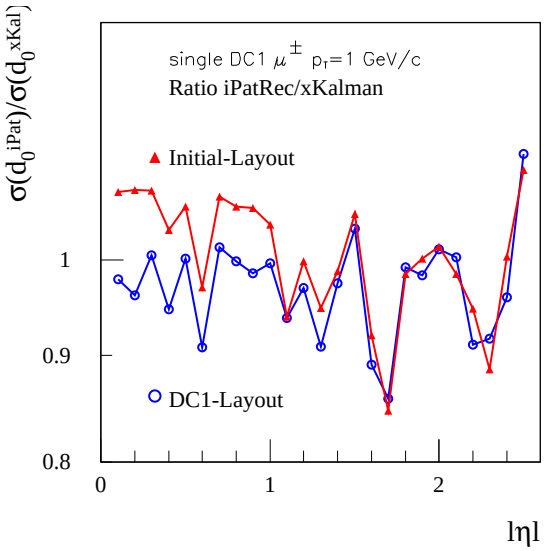

Figure 8: Ratio of d_0 resolution iPatRec to xKalman for $p_T = 1$ GeV for DC1 and Initial layout.

observation that the expected changes in resolution going from the DC1 to Initial layouts are exhibited by iPatRec but not by xKalman poses a general problem.

At high momentum the resolution is sensitive to the cluster measurement errors (see Section 3). Since iPatRec uses valid although smaller errors than xKalman it is not surprising that iPatRec obtains d_0 resolutions $\sim 10\%$ better than xKalman over all $|\eta|$ for the DC1 layout. However, for the Initial layout the iPatRec resolution is degraded due to the missing pixel layer and the reduced granularity. This is most significant in the barrel region. Although the two algorithms are seen to agree over a large fraction of the $|\eta|$ range, the agreement is fortuitous as xKalman is insensitive to changes between the two layouts. At the higher values of $|\eta|$, the reduction in the difference between ratios is due to the different geometry of the end-cap.

At low momentum, where multiple scattering dominates, the two algorithms give results in close agreement for both layouts above $|\eta| \sim 1$, as expected. The fine structure seen is due to different representations of the material distributions used by the two algorithms, mentioned in Section 3. However, when going from the DC1 to the Initial layout, iPatRec sees a degradation in resolution of 5-10% compared with xKalman in the barrel region.

The p_T dependence of the transverse impact parameter in the region $|\eta| < 0.25$, for the DC1 and Initial layouts, is shown for iPatRec in Figure 9. It is seen that the resolution of the Initial layout is 5-10% worse than that of the DC1 layout at all values of p_T studied. The data in the central $|\eta|$ region are well fitted with the parametrization of the form $A + B/p_T$, introduced in Section 4. Values of the A and B parameters together with those from a similar fit to the Physics TDR resolutions are presented in Table 2.

Transverse impact parameter resolution			
$\sigma(d_0)(\mu m)$	Initial layout	DC1 layout	TDR layout
iPatRec	$\sigma(d_0) = 11 \oplus \frac{100}{p_T}$	$\sigma(d_0) = 10 \oplus \frac{94}{p_T}$	$\sigma(d_0) = 11 \oplus \frac{73}{p_T}$

Table 2: Transverse impact parameter resolution for DC1 and Initial layout compared to TDR layout for iPatRec.

The resolutions of the DC1 and Initial layouts are significantly degraded from the TDR values at the lowest momenta. At p_T= 1 GeV/c, the deterioration is $\sim$ 30% for the DC1 layout and almost $\sim$ 40% for the Initial layout. For the Initial layout, this degradation reduces to $\sim$ 15% by 10 GeV/c.

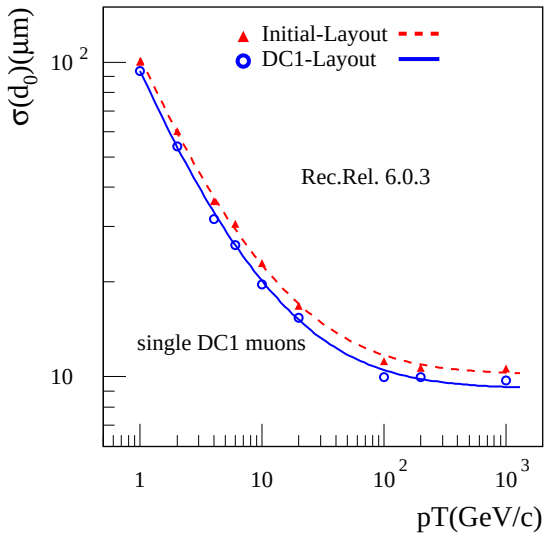

Figure 9: Transverse impact parameter resolution of charged tracks as a function of p_T for $|\eta| < 0.25$ for both layouts.

5.2 Longitudinal impact parameter resolution

The projection of z_0 onto the plane perpendicular to track direction is also an important measurement for vertexing and b-tagging. The longitudinal impact parameter resolution, $\sigma(z_0) \times sin\theta$, is shown as a function of $|\eta|$, in Figures 10 and 11, for the DC1 and Initial layout, at p_T = 1 and 200 GeV/c, for iPatRec and xKalman respectively.

As for the transverse impact parameter, the resolutions of both layouts and both algorithms show similar trends with $|\eta|$.

At high momentum the smaller clusters cause the resolution as a function of $|\eta|$ to be worst at $|\eta| = 0$, with an improvement by a factor $\sim$2 achieved by saturation at $|\eta| \sim$1. Beyond this value, there is a slow worsening of the resolution for similar reasons to the transverse impact parameter.

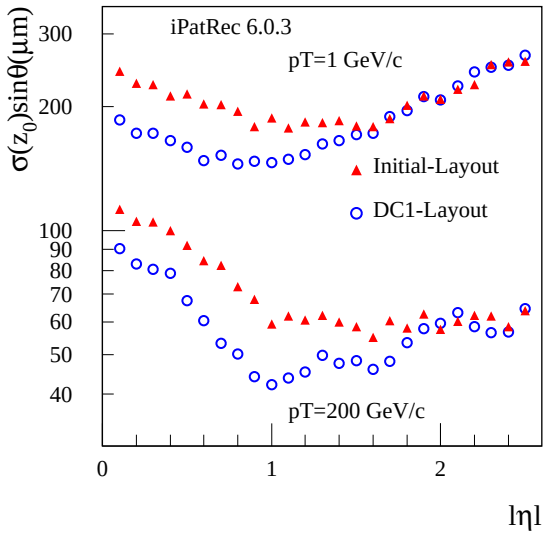

Figure 10: Longitudinal impact parameter resolution projected transversely to the track direction ($z_0 \times sin\theta$) as function of $|\eta|$ for muons of $p_T = 1$ GeV and $p_T = 200$ GeV for both layouts (iPatRec).

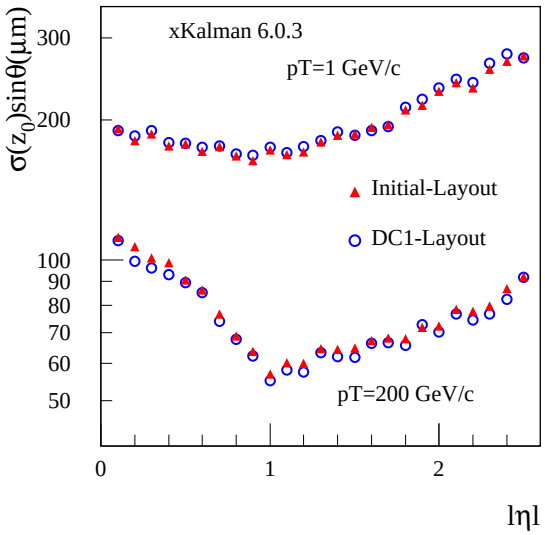

Figure 11: Longitudinal impact parameter resolution projected transversely to the track direction ($z_0 \times sin\theta$) as function of $|\eta|$ for muons of $p_T = 1$ GeV and $p_T = 200$ GeV for both layouts (xKalman).

At low momentum, in the barrel region, one again sees the improvement of resolution with $|\eta|$ due to increasing cluster size, but here the gain is offset by the corresponding increase in multiple scattering. Beyond $|\eta| \sim 1$, the multiple scattering is completely dominant.

For iPatRec, the effects of the degraded Initial layout pixel system are apparent in the barrel region at all momenta, but become insignificant at high $|\eta|$. It appears that for this result is incorrect for this version of xKalman.

The ratio of the longitudinal impact parameter resolution for iPatRec/xKalman for DC1 and Initial layouts, at $p_T = 200$ and 1 GeV/c, is shown in Figures 12 and 13.

At high momentum, for the DC1 layout, the ratio remains approximately constant over all $|\eta|$, although it shows sizable fluctuations. iPatRec finds 20-30% better resolution than xKalman. As only iPatRec is sensitive to the changed B-layer granularity when going to the Initial layout, the value of the ratio increases. The value close to unity in the barrel region is fortuitous. In the end-caps the ratios for the two layouts are in agreement as effects other than the granularity dominate. However, due to the smaller cluster errors used by iPatRec, it obtains a ∼20% better resolution.

At low momentum, there are large differences between the two algorithms for both layouts, in both barrel and overlap regions. For the DC1 layout the ratio starts at unity for $|\eta| = 0$, decreases to ∼0.85 at the end of the barrel, and then returns to approximately unity by the end of the overlap region. The two algorithms give approximately the same resolution in the end-cap region. Here again, a loss of resolution going from DC1 to Initial layout is seen by iPatRec but not by xKalman. This results in the ∼

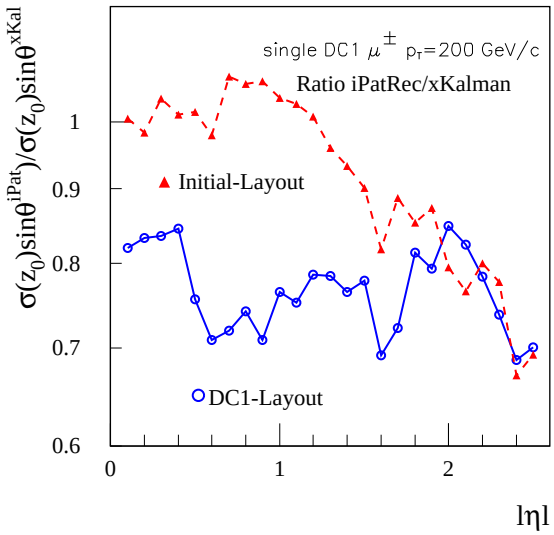

Figure 12: Ratio of Longitudinal impact parameter resolution projected transversely to the track direction ($z_0 \times sin\theta$) iPatRec to xKalman for p_T =200 GeV for DC1 and Initial layout.

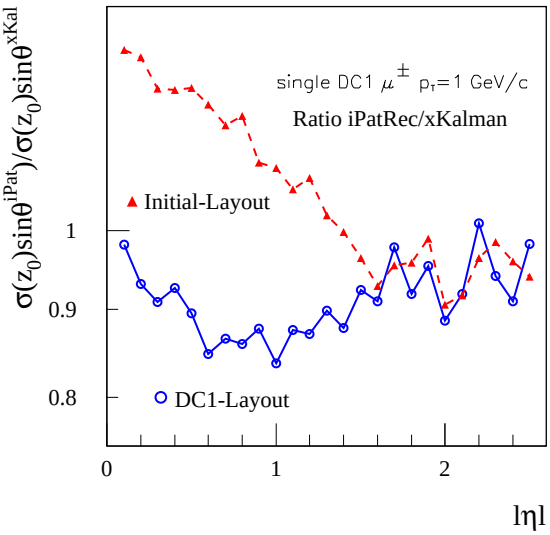

Figure 13: Ratio of Longitudinal impact parameter resolution projected transversely to the track direction ($z_0 \times sin\theta$) iPatRec to xKalman for p_T =1 GeV for DC1 and Initial layout.

20% decrease of the ratio in the barrel region compared to the DC1 ratio.

The resolution measured by iPatRec at high momentum for the DC1 layout is in close agreement with the value shown in the physics TDR, in the barrel region. This is expected as the longitudinal impact parameter resolution is detector error dominated, and the detector element dimensions are the same. The resolution degrades somewhat from the TDR value in the end-caps for the reasons already discussed.

5.3 Inverse transverse momentum resolution

The resolution of the inverse transverse momentum, p_T, expressed as a function of $|\eta|$, for the DC1 and Initial layouts, at p_T = 1 and 200 GeV/c, is shown for iPatRec and xKalman in Figures 14 and 15 respectively.

The two layouts show similar results at both momenta, with the two algorithms in close agreement.

At high p_T, the resolution is fairly constant up to $|\eta| \sim 1.5$, except for a bump around $|\eta| \sim 0.8$ corresponding to the TRT barrel-forward transition region where there are fewer straws. For higher values of $|\eta|$ the resolution becomes progressively worse due to the reduction in radial track length, and the reduction in magnetic field integral resulting from the finite length of the solenoid. A degradation of the resolution from the value obtained with the Physics TDR layout above $|\eta| \sim 1.5$, is due to a poorer measurement of the track sagitta, caused by the displacement, down-sizing and removal of detector layers from the TDR layout.

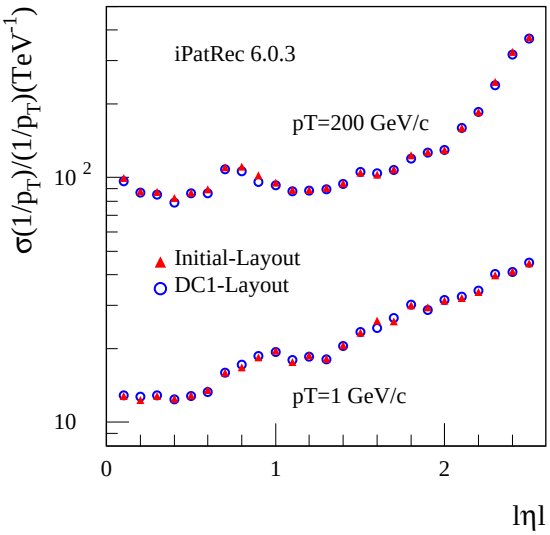

Figure 14: Inverse transverse momentum ($1/p_T$) resolution(compared to MCTruth) as function of $|\eta|$ for muons of $p_T = 1$ GeV and $p_T = 200$ GeV for both layouts (iPatRec).

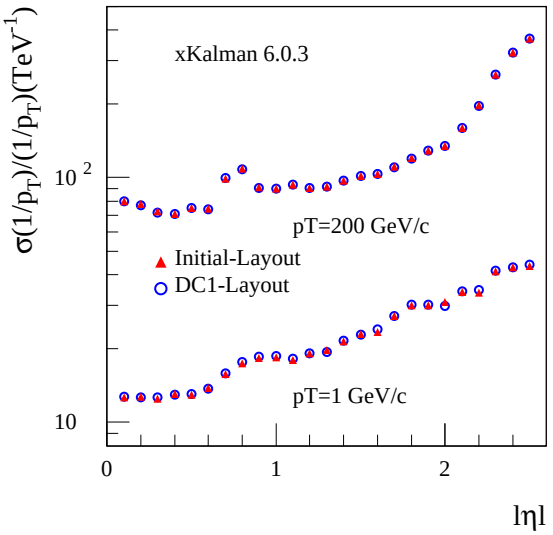

Figure 15: Inverse transverse momentum ($1/p_T$) resolution(compared to MCTruth) as function of $|\eta|$ for muons of $p_T = 1$ GeV and $p_T = 200$ GeV for both layouts (xKalman).

Multiple scattering dominates the resolution at low p_T. The continuous increase of material with $|\eta|$ produces a corresponding degradation of the resolution. In addition, the material in the support/service structure at the end of the barrel adds to the effect of fewer TRT straws in this region. At high $|\eta|$ the effects of reduced radial track length and reduced field integral are apparent but less severe than at high momentum. However, there is a further worsening of the resolution due to the extra material introduced by the insertable pixel support cylinder.

The ratio of the $1/p_T$ resolution for iPatRec/xKalman for DC1 and Initial layouts, at p_T= 200 and 1 GeV/c, is shown in Figures 16 and 17

At high momentum, in the overlap and end-cap regions, the two layouts give similar results, but in the barrel region iPatRec is $\sim 20\%$ worse. A broadening of the corresponding fit pull in this region indicates that this is due to a problem with iPatRec, which appears to be related to the treatment of the TRT detector description.

At low momentum, where multiple scattering dominates, the two algorithms and the two layouts give similar resolutions at all $|\eta|$.

The p_T dependence of the $1/p_T$ resolution integrated over all $|\eta|$, for the DC1 and Initial layouts, is shown for iPatRec in Figure 18. Similar values are obtained with xKalman. Both layouts give results in close agreement at all values of p_T. The data are well fitted with a parametrization of the the form:

$$A + \frac{B}{p_T \times \sqrt{\sin\theta}} \tag{7}$$

Values of the A and B parameters are presented in Table 3 for the DC1, Initial and

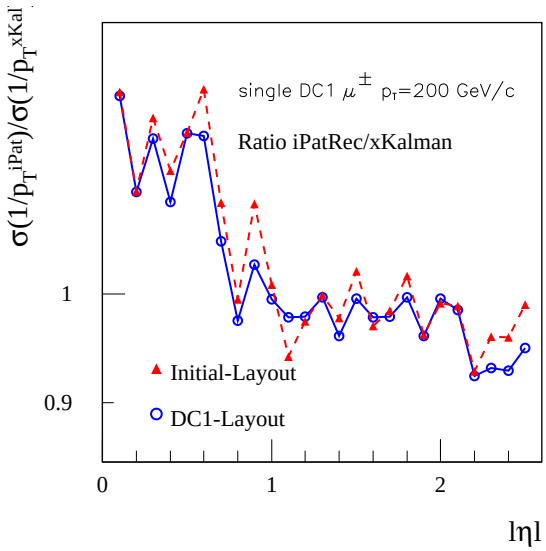

Figure 16: Ratio of $1/p_T$ resolution iPatRec to xKalman for p_T = 200 GeV for DC1 and Initial layout.

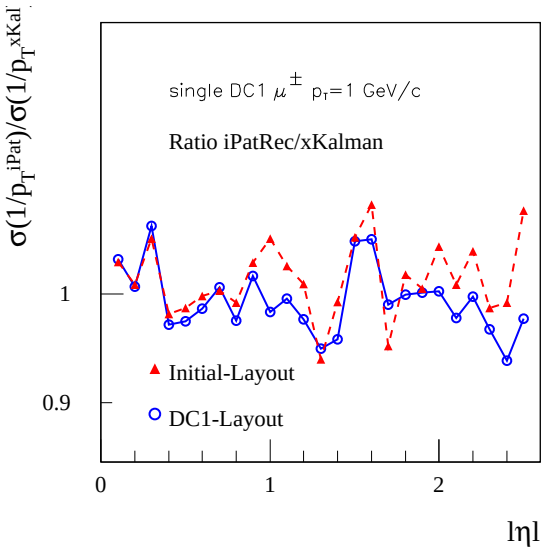

Figure 17: Ratio of $1/p_T$ resolution iPatRec to xKalman for $p_T = 1$ GeV for DC1 and Initial layout.

Inverse transverse momentum resolution			
$\sigma(\frac{1}{p_T})(TeV^{-1})$	Initial layout	DC1 layout	TDR layout
iPatRec	$\sigma(\frac{1}{p_T}) = 0.56 \oplus \frac{22}{p_T\sqrt{sin\theta}}$	$\sigma(\frac{1}{p_T}) = 0.55 \oplus \frac{22}{p_T\sqrt{sin\theta}}$	$\sigma(\frac{1}{p_T}) = 0.36 \oplus \frac{13}{p_T\sqrt{sin\theta}}$

Table 3: Inverse transverse momentum resolution for DC1 and Initial layout compared to TDR layout for iPatRec.

TDR layouts.

Due to the increased radius of the B-layer and the presence of more material, the resolution is significantly degraded from the TDR value. Both the intrinsic error coefficient, A, and the multiple scattering coefficient, B, are modified, A increasing by ∼50%, and B by ∼70%.

5.4 Pull Distributions and Tails

The quality of the track fit to the perigee parameters has been looked at by measuring the pulls and the tails of the distributions. This has only been performed for the DC1 layout because there is insufficient data available for the Initial layout. The final fits exhibit Gaussian peaks with non-Gaussian tails arising from low quality tracks. Pull distributions measuring the quality of the peaks were obtained by refitting the original distributions after making cuts at $\pm 3\sigma$. The $\pm 3\sigma$ tails were then used as a measure of the bad quality tracks.

The mean of the pull distributions for the fitted parameters, d_0, z_0,$1/p_T$, ϕ and $cot\theta$, is

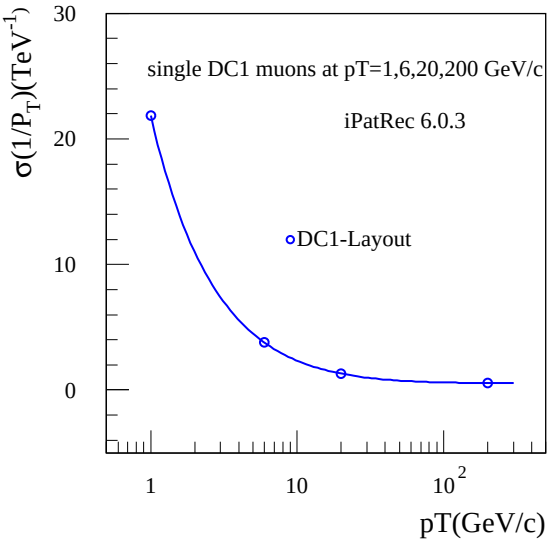

Figure 18: Inverse transverse momentum resolution of charged tracks as a function of p_T in $|\eta| < 2.5$ for DC1 layout (iPatRec). The resolution plot for the Initial layout is identical.

shown for the iPatRec and xKalman algorithms at four representative momenta, separately for the barrel and end-cap regions, in Tables 4 and 5 respectively. Almost all the distributions are seen to be well-centered apart from the xKalman $1/p_T$ measurements at the highest momentum (200 GeV/c).

The width of these pull distributions is shown in Tables 6 and 7 for the barrel and end-cap regions. The majority are compatible with the expected width of unity. However, iPatRec exhibits a broadening of the p_T and ϕ widths at high momentum in the barrel region indicating that the fitted errors are underestimated. As previously mentioned, this is believed to be due to some inaccuracies in the treatment of the TRT. The $cot\theta$ distribution from xKalman is too broad at high momentum in the barrel and end-cap. Both programs overestimate the error on the impact parameter at high momenta.

As the above problems mainly occur when measurement error dominates, it is to be hoped that the new EDM and detector description developments will provide more correct values and error estimates for the individual clusters and TRT hits.

The 3 σ tail fractions for the five perigee parameter pull distributions are presented as a function of p_T in Figure 19. Again, numbers are given for the DC1 layout, for iPatRec and xKalman, and for the barrel and end-caps separately.

It is seen that iPatRec has smaller tail fractions than xKalman for all parameters at all values of p_T, the differences varying by up to a factor of 10. xKalman itself has similar tail fractions in barrel and end-caps, and shows little variation with p_T except for the $1/p_T$ parameter. iPatRec also finds reasonable agreement between barrel and end-caps except for the longitudinal parameters, z_0 and $cot\theta$. Both algorithms show similar trends as a function of p_T, with the exception of the highest value of p_T. Since the differences between the programs are so large, it is important that they continue to be monitored during the introduction of the new common EDM.

$p_T(GeV/c)$		d_0	z_0	$1/p_T$	ϕ	$\cot\theta$
1	$iPatRec$	0.01	0.00	0.00	0.00	0.00
	$xKalman$	-0.01	0.00	0.04	0.02	0.00
6	$iPatRec$	0.03	-0.02	-0.02	-0.02	0.00
	$xKalman$	0.02	-0.02	0.06	0.00	0.00
20	$iPatRec$	0.06	0.00	0.00	-0.03	0.00
	$xKalman$	0.03	-0.02	0.04	-0.01	0.01
200	$iPatRec$	0.09	0.02	0.00	-0.07	-0.02
	$xKalman$	0.03	-0.02	**0.20**	-0.03	-0.08

Table 4: Mean of the Pull distributions for iPatRec and xKalman in the barrel region ($|\eta| < 0.8$), for DC1 layout.

$p_T(GeV/c)$		d_0	z_0	$1/p_T$	ϕ	$\cot\theta$
1	$iPatRec$	0.03	0.00	-0.01	-0.02	0.00
	$xKalman$	0.00	0.00	-0.02	0.00	0.00
6	$iPatRec$	0.00	0.00	0.03	0.00	0.01
	$xKalman$	0.00	-0.02	0.00	0.00	0.02
20	$iPatRec$	0.00	0.00	0.04	0.02	0.00
	$xKalman$	0.00	0.00	0.04	0.00	0.00
200	$iPatRec$	0.00	0.00	0.04	0.03	0.02
	$xKalman$	-0.03	-0.03	**0.11**	0.05	0.00

Table 5: Mean of the Pull distributions for iPatRec and xKalman in the endcap region ($1.6 < |\eta| < 2.5$), for DC1 layout.

$p_T(GeV/c)$		d_0	z_0	$1/p_T$	ϕ	$\cot\theta$
1	$iPatRec$	0.96	0.99	**1.15**	1.02	1.01
	$xKalman$	0.97	1.02	1.07	1.07	1.08
6	$iPatRec$	1.00	0.97	1.06	1.01	0.99
	$xKalman$	0.95	1.00	0.99	1.05	1.02
20	$iPatRec$	1.05	0.96	1.08	1.05	0.95
	$xKalman$	**0.86**	0.99	0.96	1.03	0.98
200	$iPatRec$	1.08	0.95	**1.31**	**1.18**	0.93
	$xKalman$	**0.82**	1.05	1.03	1.07	**1.14**

Table 6: Sigma of the Pull distributions for iPatRec and xKalman in the barrel region ($|\eta| < 0.8$), for DC1 layout.

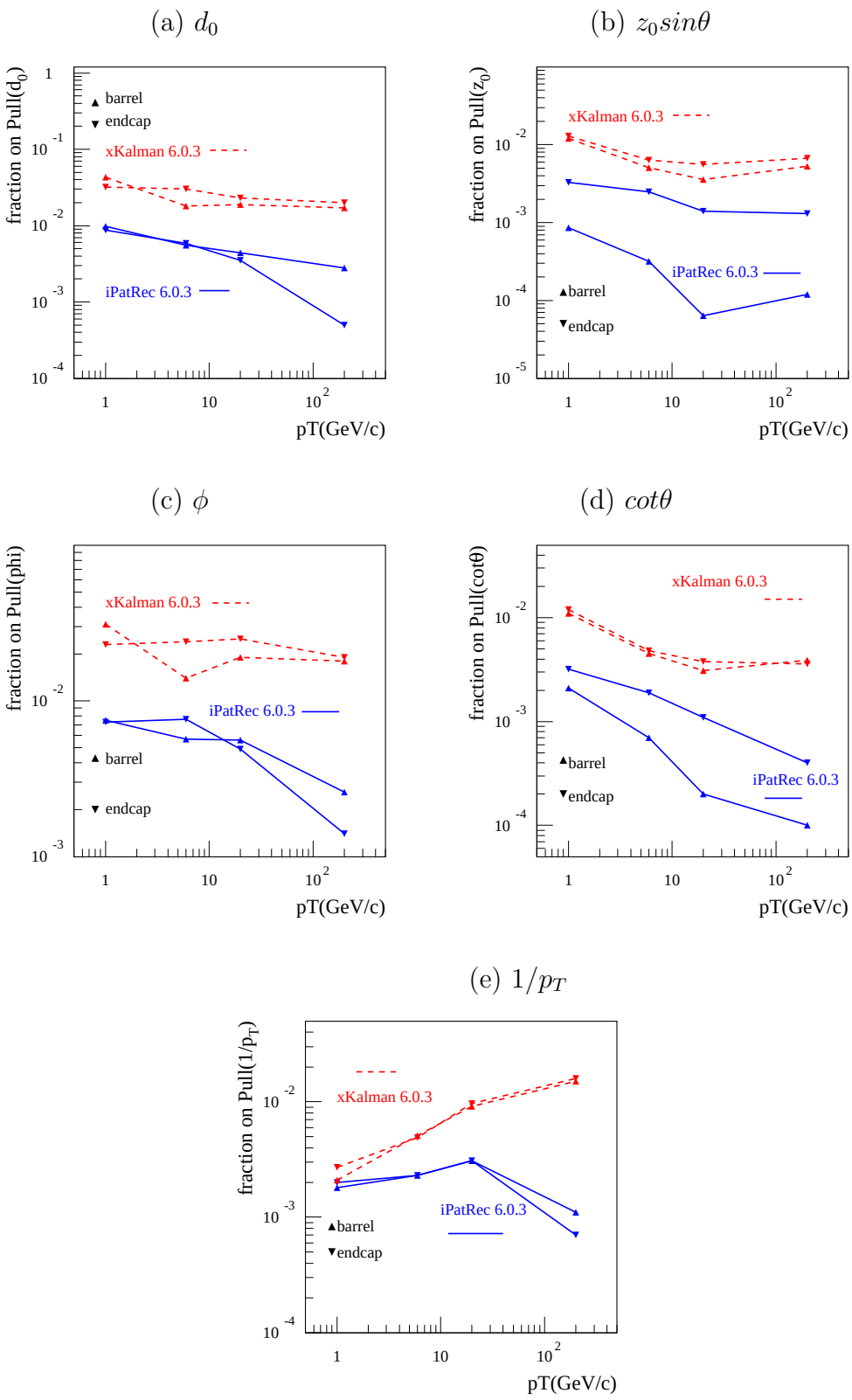

Figure 19: (a), (b), (c), (d), (e):Tail fractions for d_0, z_0, ϕ, $cot\theta$ and $1/p_T$ as a function of p_T for iPatRec and xKalman for barrel and end-cap regions (DC1 layout) .

$p_T(GeV/c)$		d_0	z_0	$1/p_T$	ϕ	$\cot\theta$
1	$iPatRec$	0.98	0.95	1.09	1.05	1.00
	$xKalman$	1.09	1.04	1.06	**1.17**	**1.16**
6	$iPatRec$	**0.88**	1.01	1.05	0.97	1.04
	$xKalman$	0.93	0.93	1.02	1.09	1.08
20	$iPatRec$	**0.88**	1.02	0.98	**0.89**	1.01
	$xKalman$	**0.89**	**0.89**	0.99	1.07	1.04
200	$iPatRec$	**0.87**	1.02	1.09	1.01	1.01
	$xKalman$	**0.81**	0.96	1.05	1.05	**1.20**

Table 7: Sigma of the Pull distributions for iPatRec and xKalman in the end-cap region ($1.6 < |\eta| < 2.5$), for DC1 layout.

5.5 Track Efficiencies

The reconstruction efficiency for muons is a measure of the optimum single particle efficiency. Pions and electrons have their efficiency reduced by hadronic interactions and bremsstrahlung, respectively.

The single track reconstruction efficiencies for muons and pions, are shown as a function of p_T, in Figures 20, 21, and 22, 23, separately for the barrel region ($|\eta| < 0.8$), and end-cap region ($1.6 < |\eta| < 2.5$). The results from the two algorithms are in quite good agreement in both regions and at all momenta.

Muons have an overall efficiency ∼99.5% with losses due to the simulated detector inefficiency and a slight lack of hermeticity in the end-cap region. The performance differences seen earlier between the iPatRec and xKalman algorithms cannot be attributed to relative track finding inefficiences.

Pion efficiencies are about 5 to 10% lower than muon efficiencies due to interactions. Three interaction categories can be distinguished; early, intermediate and late. Late interactions, which occur towards the outside of the inner detector, have full efficiency but a loss of resolution from the shorter measured length. Early interactions, which occur in the beam-pipe or Pixel detector, cannot be found because there are too few measurements to define the track. The intermediate category have insufficient correct hits to satisfy the quality criteria, but are nevertheless found when the pattern recognition wrongly associates one or more downstream hits from leading secondary particles. The probability of this occurrence, hence the measured efficiency, increases with momentum. The effect is more pronounced at high $|\eta|$ because of the interactions in the barrel support/service structure in front of the end-cap SCT detectors with the rise shifted to a lower p_T value. Of course, these 'extra' tracks have badly measured parameters.

Electron efficiencies are lower than for muons due to catastrophic bremsstrahlung energy losses. However, the major effect of bremsstrahlung is to distort the fitted parameters in the bending plane. In particular, the momentum tends to be underestimated.

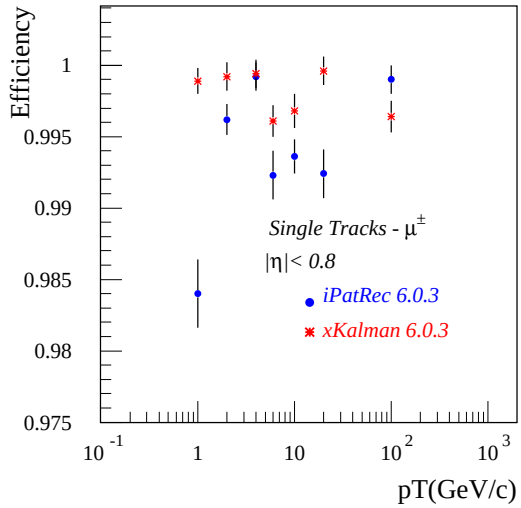

Figure 20: Single muon track efficiency as a function of p_T in the barrel region.

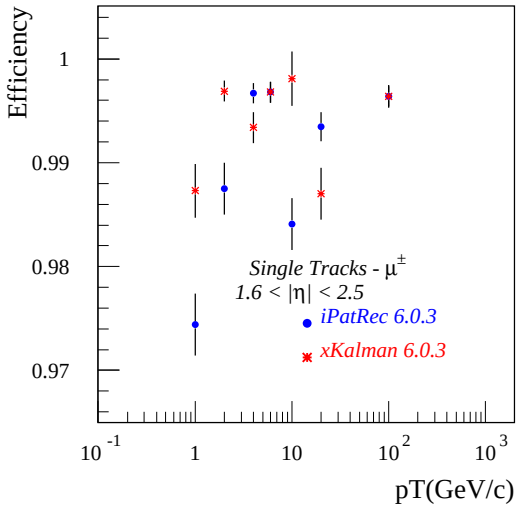

Figure 21: Single muon track efficiency as a function of p_T in the end-cap region.

6 Tracks in Jets

Studies of the tracking with jets complement the studies with single particles. Whereas single particles provide a measure of the ultimate detector performance and give resolutions which can be used for physics analyzes, studies of the tracking with jets are much more demanding and indicate the limitations of the overall detector design. Obviously the performance of the pattern recognition depends critically on the density of tracks in a jet, and hence its energy.

Two important parameters to study here are the efficiency for finding tracks in jets and the quality of the tracks. This section looks at these parameters for DC1 di-jets. and makes a systematic comparison between the iPatRec and xKalman algorithms and the DC1 and Initial layouts. Fully simulated di-jet events with $p_T > 17, 35, 70, 140, 280, 560$ GeV/c at the parton level, with $|\eta| < 2.7$, have been used. Studies have been made for basic jets and with 2 levels of pile-up. Tracks within a cone of ΔR= 0.4 around each jet, and with $p_T > 1$ GeV/c have been reconstructed.

For these studies the radius and half length of the origin vertex have been restricted to be less than 30 cm and 150 cm respectively.

6.1 Pull distributions

The quality of the tracks found in jets has been studied by measuring the pulls of the impact parameter and transverse momentum distributions. Gaussian fits to the distributions were made after $\pm 3\sigma$ cuts, as for single particles.

The mean and sigma of these pull distributions as a function of Pt are shown in Figures 24 and 25, respectively. Results are presented for the DC1 and Initial layouts, for both

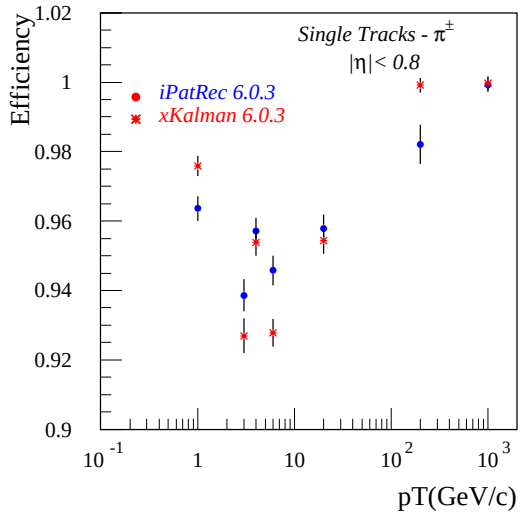

Figure 22: Single pion track efficiency as a function of p_T in the barrel region.

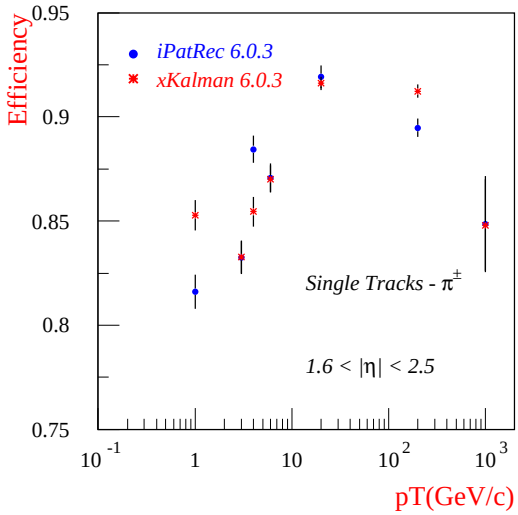

Figure 23: Single pion track efficiency as a function of p_T in the end-cap region.

algorithms, separately for the barrel and end-cap regions.

For all combinations of algorithm and layout the fluctuations of the mean value lie within approximately $\pm$ 5%, and no major variations with p_T are visible. The only significant offset of the average value of the mean occurs for the longitudinal impact parameter, where shifts of ~ 0.1 are seen for the Initial layout. These values suggest an error in the Event Data Model(EDM) or the detector description for the Initial layout.

The values of sigma for the transverse impact parameter are reasonably well behaved for both algorithms and both layouts. However, the errors are overestimated, particularly in the end-cap region, for the longitudinal impact parameter, but underestimated for the transverse momentum. Although the errors here are incorrect at the 10% level for jets, they were previously seen to be correct for single muons. This effect is interpreted as the result of interactions in the material of the detector which produce secondary pions of lower momentum and hence wrong hits. For the longitudinal impact parameter, the approximately 30% overestimate of the end-cap error seen by both algorithms and both layouts, is not understood.

The tail fractions of the pull distributions as a function of p_T for d_0, $1/p_T$, $z0 \times sin\theta$ for the 2 algorithms, the 2 layouts, and for barrel and end-cap regions are shown in Figure 26.

A first observation is that all tail fractions increase with momentum. Since the track momentum increases towards the center of a jet where there is a corresponding increase of the number of wrong hits picked up on a track, the tail fraction of the pull also increases with momentum. This phenomenon was observed and discussed in the physics TDR[5]. It is contrary to the behavior of the tail distributions for single muons which in general show a fall with p_T.

The tail fractions found here in jets are somewhat larger than for single muons, even at low p_T.

It is seen that the tail fraction for both layouts is larger by up to an order of magnitude for xKalman than for iPatRec. Such an effect is also present in the single muon results.

A final observation is that there is not much difference in the tail fractions between the two layouts or between the barrel and end-cap regions.

6.2 Overall performance

The number of signal tracks per event above $p_T = 1$ GeV/c for DC1 di-jets, averaged over all $|\eta|$, is shown as a function of jet p_T in Figure 27. Results are presented for the DC1 layout using the iPatRec and xKalman algorithms, with and without the addition of pile-up events.

There is no apparent increase in the number of tracks found with the addition of low luminosity pile-up, although with high luminosity pile-up the number increases by $\sim$ 10% at the lower momenta and 20% at 500 GeV/c. Both algorithms give similar results. It is seen that the appearance of background tracks above $p_T = 1$ GeV/c, only becomes significant with the highest levels of pile-up, and even then the levels are relatively small.

The mean value of track $|p_T|$ as a function of the jet p_T, for DC1 and Initial layouts, for iPatRec and xKalman algorithms is shown in Figure 28. There is a logarithmic rise of the mean p_T with jet p_T away from threshold. The differences between the two layouts and the two algorithms are small, with a maximum discrepancy of 5% at $p_T =$ 500 GeV/c.

The reconstruction efficiency for tracks in jets is a further parameter of interest. A track is classified as primary if it has a small transverse impact parameter and a sufficient number of hits in the vertex region and secondary if it fails these criteria. The reconstruction efficiency for finding primary and secondary tracks as a function of the jet p_T for the iPatRec and xKalman algorithms is shown in Figures 29 and 30 for barrel and end-cap regions respectively.

The two algorithms are in close agreement for primary tracks in both barrel and end-cap regions. In the barrel region the efficiency is $\sim$ 92%, degrading to $\sim$ 85% in the end-caps due to the presence of more material. For secondaries, xKalman is 20 - 30% more efficient than iPatRec. The reasons for this are not understood. There is a need for more work and more studies in this area.

A comparison of the reconstruction efficiencies for primary tracks alone, and with low $(2 \cdot 10^{33} cm^{-2} s^{-1})$ and high $(10^{34} cm^{-2} s^{-1})$ luminosity pile-up, are shown in Figures 33 and 34 for the barrel and end-cap regions respectively.

No consistent pattern of variation with momentum is apparent for either of the algorithms. Moreover the presence of pile-up does not change the efficiency by more than $\sim$ 5%.

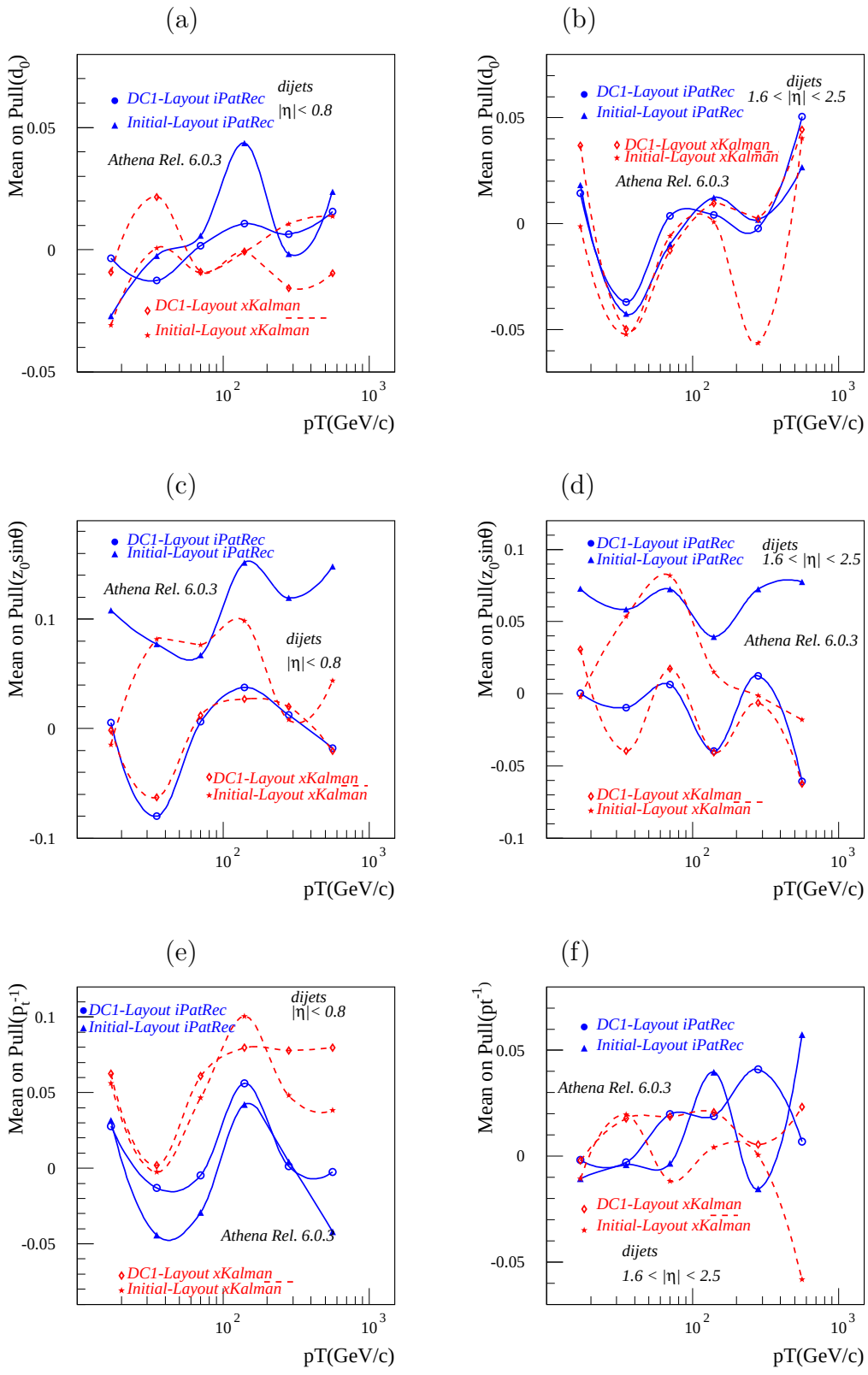

Figure 24: Comparison of the mean on the pull distributions : $Pull(d_0)$(a)-(b), $Pull(z_0 \times sin\theta)$(c)-(d), $Pull(1/p_T)$(e)-(f) for barrel and end-cap respectively.

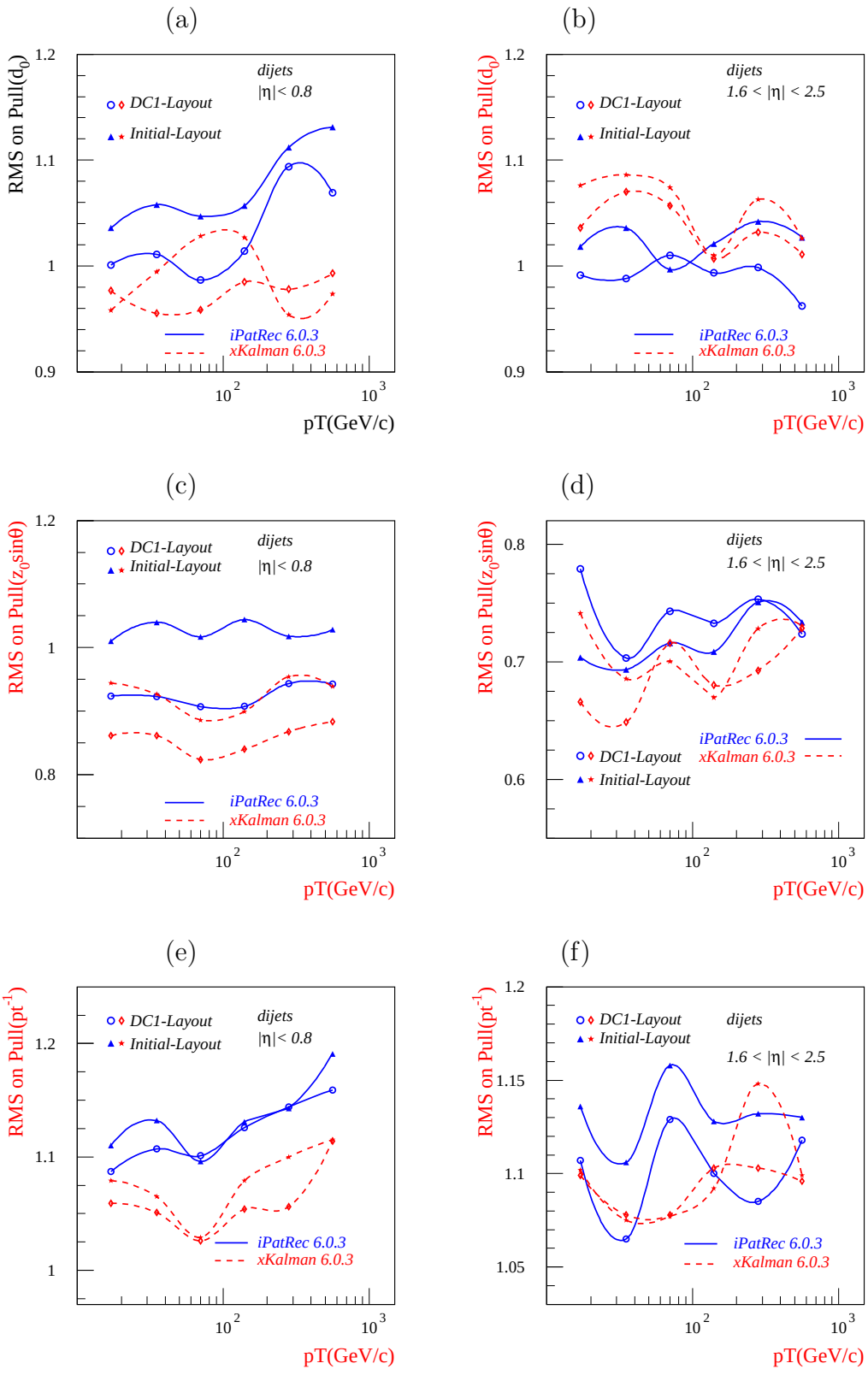

Figure 25: Comparison of the width of the pull distributions : $Pull(d_0)$(a)-(b), $Pull(z_0 \times sin\theta)$(c)-(d), $Pull(1/p_T)$(e)-(f) for barrel and end-cap respectively.

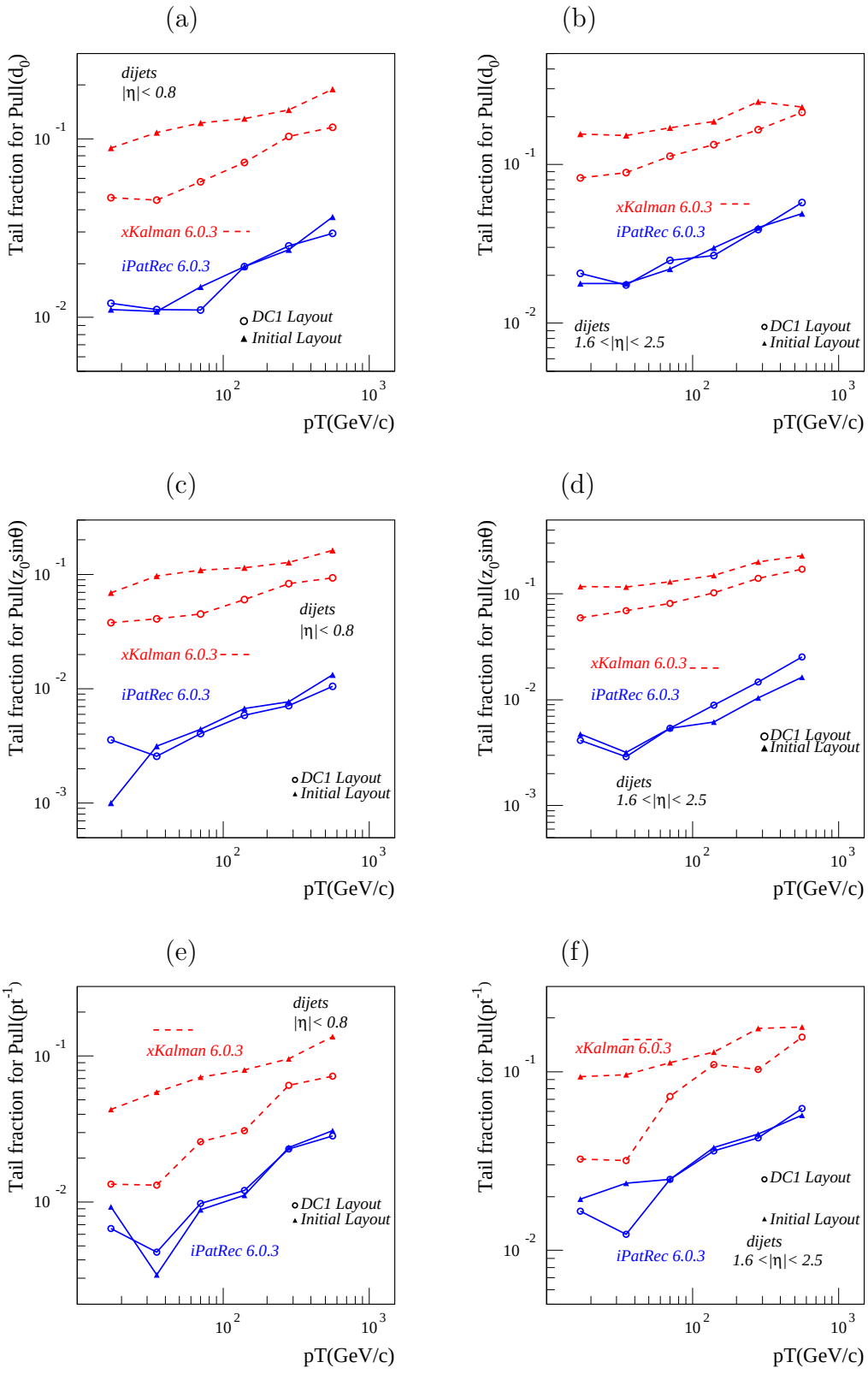

Figure 26: Tail fraction for d_0(a)-(b), $z_0 \times sin\theta$(c)-(d), $1/p_T$(e)-(f) pulls for barrel and endcap respectively.

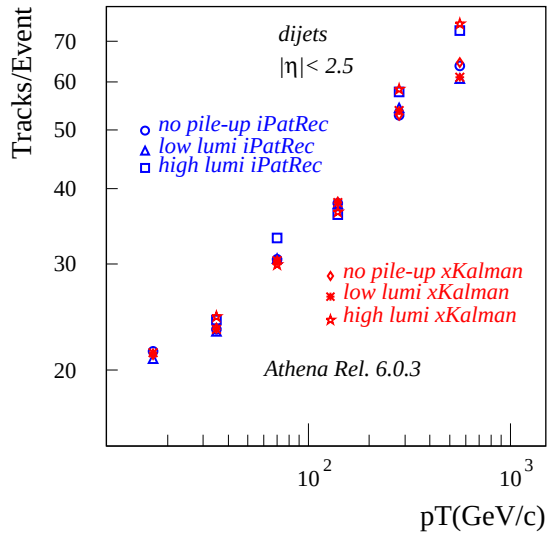

Figure 27: Signal tracks per event with $p_T > 1$ GeV/c.

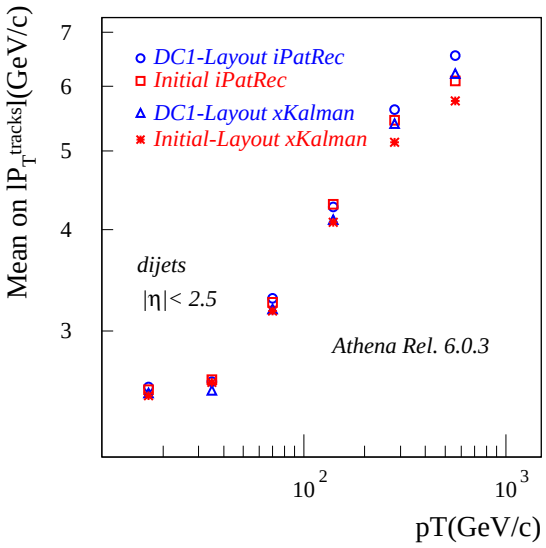

Figure 28: Mean on track $|p_T|$ versus p_T jet threshold.

7 Conclusions

The track finding and measuring capabilities of the ATLAS Inner Detector have been studied using the reconstruction software available within the Athena framework. Impact parameter and transverse momentum resolutions have been obtained for single muons and tracks in jets, with and without the addition of pile-up. The efficiency of the track finding and the quality of the resultant tracks has also been studied. Results have been derived using two reconstruction packages, iPatRec and xKalman, and two layouts, the so-called DC1 and Initial layouts. Some of the results have been compared with those in the physics TDR[3].

It has been shown that the two packages are able to accurately identify and reconstruct tracks, including pile-up, in the Inner Detector. The input data used, including material distributions, detector descriptions, noise and detector inefficiency was as accurate a representation of the final data as present knowledge permits. The correct inhomogeneous magnetic field was also used. Obviously the packages are still missing some final items such as the capability to handle calibration and alignment data, and the ability to output persistent results. It should also be noted that both packages are able to operate at an acceptable event processing rate, processing jets with pile-up at a rate well inside the specifications given in the Computing Technical Proposal[6].

Both algorithms give comparable results overall, although several differences of detail exist. Some of these differences, such as the sensitivity to recent pixel layout modifications, are attributed to the different sources of input data used by the two algorithms. The availability of independent algorithms has facilitated the validation of the results, and the existence of a second algorithm has been to their mutual benefit during the development stages. A few outstanding differences between the algorithm performances remain to be understood.

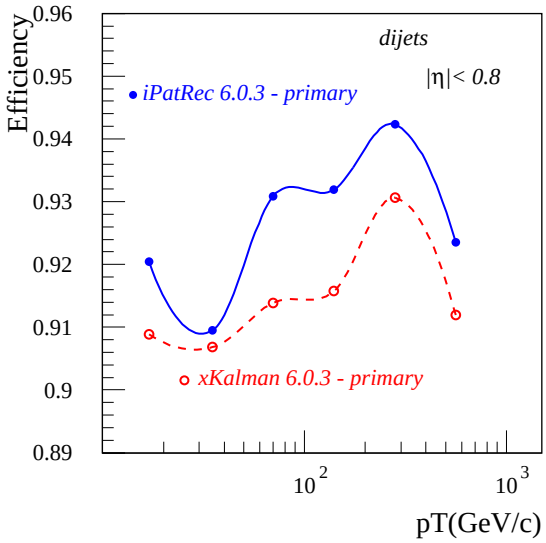

Figure 29: Reconstruction efficiency for primary tracks in the barrel region $|\eta| < 0.8$ as a function of track p_T.

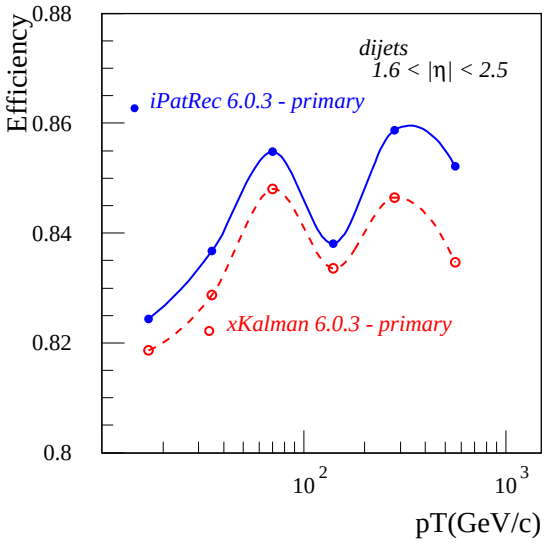

Figure 30: Reconstruction efficiency for primary tracks in the end-cap region $1.6 < |\eta| < 2.5$ as a function of track p_T.

Both algorithms find the resolutions for the DC1 layout to be degraded from those of the physics TDR layout. This was expected, as a result of the introduction of more material and a poorer measurement of the track due to an increase in pixel size and a shift of detectors to less optimum radii. The loss of transverse impact parameter resolution was found to be $\sim 30\%$ in the barrel and $\sim 50\%$ in the end-caps, while the loss of momentum resolution was found to be $\sim 40\%$ in the barrel and $\sim 60\%$ in the end-caps.

A degradation of the results for the Initial layout compared with the DC1 layout has also been observed. By itself, the removal of the intermediate pixel layer does not have much affect on the resolutions. However, when detector inefficiency is present, some tracks end up with only a single associated pixel cluster, which does worsen the resolution. A further loss of resolution is caused by the reduction in B-layer granularity which affects the impact parameter and angular resolutions at all energies, but does not worsen the momentum resolution.

The quality of the reconstructed tracks has been measured by making Gaussian fits to the pull distributions of the track perigee parameters. Fit means and sigmas have shown that the track quality is good for both algorithms and both layouts. However, the tails show up some notable differences between the two algorithms.

It is found that the presence of pile-up, even at high luminosity, has little effect on the track finding efficiency.

The numbers presented here are a measure of the performance of the currently foreseen ATLAS Inner Detector and update those given in the physics TDR[3]. There has been a significant degradation in resolution as a result of the subsequent geometrical modifications and the addition of more material.

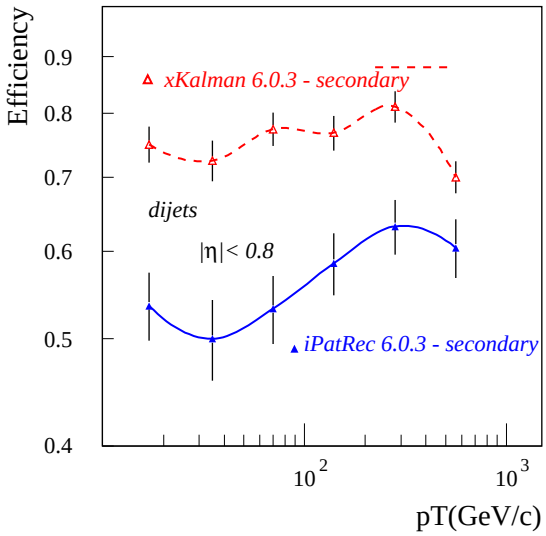

Figure 31: Reconstruction efficiency for secondary tracks in the barrel region $|\eta| < 0.8$ as a function of track p_T.

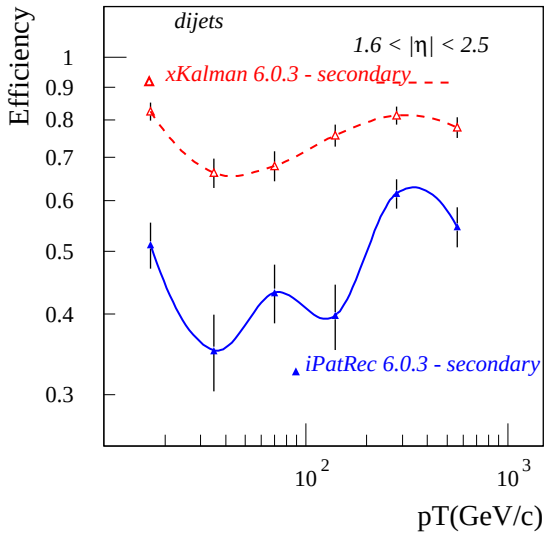

Figure 32: Reconstruction efficiency for secondary tracks in the end-cap region $1.6 < |\eta| < 2.5$ as a function of track p_T.

References

[1] R. Clifft, A. Poppleton, *IPATREC:Inner Detector pattern recognition and track fitting*, **ATL-SOFT-94-009 .**

[2] I. Gavrilenko, *Description of Global Pattern Recognition Program (XKalman)*, **ATL-INDET-97-165 .**

[3] Atlas Collaboration *ATLAS Detector and Physics Performance, Technical Design Report, Section3,* **CERN/LHCC/99-14**(1999).

[4] Atlas Collaboration *Pixel Detector, Technical Design Report*, **CERN/LHCC/98-13**(1998).

[5] Atlas Collaboration *Inner Detector, Technical Design Report, Vol.I* **CERN/LHCC/97-16**(1997).

[6] ATLAS Computing Tecnical Proposal, http://atlas.web.cern.ch/Atlas/GROUPS/SOFTWARE/TDR/html/Welcome.html

[7] ATLSIM Manual, http://atlas.web.cern.ch/Atlas/GROUPS/SOFTWARE/DOCUMENTS/simulation.html

[8] ATHENA Framework Manual, http://atlas.web.cern.ch/Atlas/GROUPS/SOFTWARE/OO/architecture/General/index.html

[9] Requirements for an Inner Detector Event Data Model, **ATLAS-ID-2002-008 .**

[10] ZEBRA, CERN Program Library **Q100** .

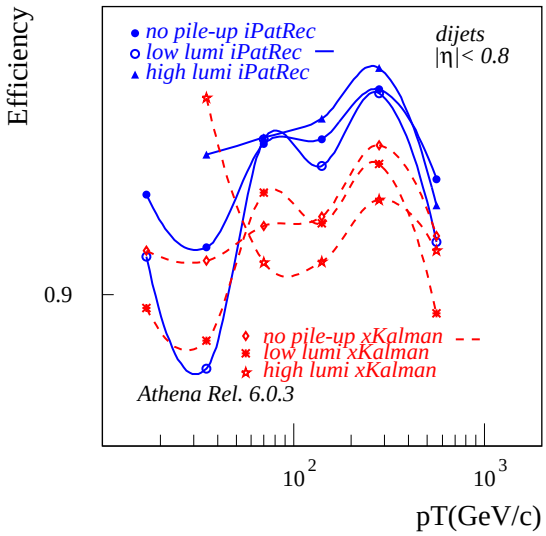

Figure 33: Reconstruction efficiency for primary tracks, with and without pileup, in the barrel region $|\eta| < 0.8$ as a function of track p_T.

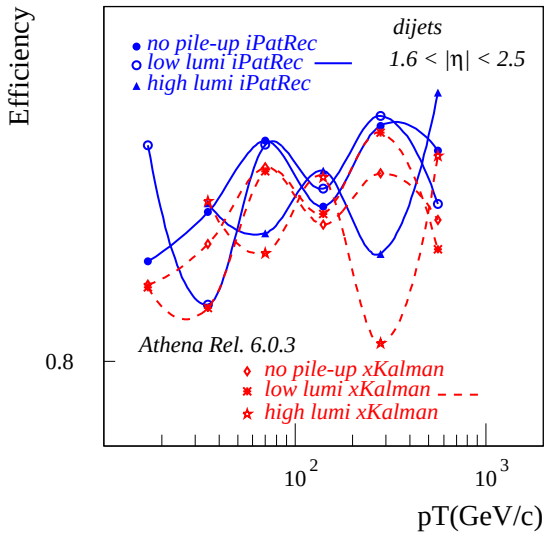

Figure 34: Reconstruction efficiency for primary tracks, with and without pileup, in the end-cap region $1.6 < |\eta| < 2.5$ as a function of track p_T.

[11] F. Tartarelli and N. Labanca, *Parameterizations for ATLFAST*, Presentation given at ATLAS B-physics meeting of 18 Neovember 1997.

[12] R.L. Gluckstern, *Uncertainties in Track Momentum and Direction due to multiple scattering and measurements errors,* Nucl. Inst. and Meth. **24**(1963) 381.